Forward Modeling for the Fine Detection of Geological Abnormal Area in Coal Seams Using High-frequency Radio Imaging Method

Shun Yang, Yanqing Wu, Peng Lu, and Zhifang Liu

***Abstract*—The radio imaging method (RIM) can be used in underground mines to identify geologically hazardous areas; however, it does not yield accurate results. To address this issue, a high-frequency (1–8 MHz) RIM is proposed here for the fine detection of geological anomalies in coal seams, and its feasibility is evaluated. A reliable forward model is established based on the propagation characteristics of electromagnetic waves in lossy media and the functional relation between the electrical parameters of coal and electromagnetic wave frequency. Numerical simulations were performed using a frame antenna at high frequencies; the field strengths of electromagnetic waves in coal seams with and without geological abnormal areas were compared. The difference diagram demonstrates the field strength attenuation "shadow area" formed by the geological abnormal area. The attenuation coefficient, wavelength, and far-field radiation characteristics of the frame antenna were used to discuss if the detected geologically hazardous location is accurate. The feasibility of high-frequency detection is further supported by the electromagnetic wave signal strength in the receiving tunnel.**

***Index Terms*—Electrical parameters, fine detection, forward modeling, high-frequency radio imaging method (RIM), numerical simulation.**

I. Introduction

GEOLOGICAL hazards resulting from coal mining are a significant global concern, and geophysical prospecting methods are widely used for predicting such hazards [1], [2], [3], [4], [5]. To ensure safety and precision in underground coal mining, geologically hazardous areas must be accurately identified [6], [7]. Underground radio imaging method (RIM) is a portable and widely used noncontact method that has the potential to be an effective detection method for intelligent unmanned mines in the future [8], [9], [10], [11].

In 1984, Hill [12] introduced a waveguide model for the RIM and derived a theoretical formula for electromagnetic wave propagation in layered media. Wait [13] derived a general mode equation for computing the propagation constant of inhomogeneous bounding rock media. Wu [14] studied the interbedded geoelectric model of coal seams and developed a method for calculating the electromagnetic wave field strength within the model. They also presented a practical algorithm for far-field magnetic field strength and designed a specialized frame antenna based on the radiation characteristics and explosion-proof requirements of coal mines. Li and Smith [15] employed the radio frequency module in COMSOL to investigate the propagation mode of underground electromagnetic waves around geological abnormal areas using the finite element method (FEM). Their study confirmed the utility of the COMSOL model for analyzing the propagation characteristics and imaging methods of underground electromagnetic waves. They also established a three-dimensional finite element model to examine the characteristics of the underground electromagnetic field and used the amplitude and phase data to evaluate the imaging capability of the underground electromagnetic wave penetration detection method. In addition, they applied the contrast source inversion method to cross-hole electromagnetic wave penetration imaging data for theoretical and practical research [16], [17], [18], [19]. Yue [20] studied the field strength and phase characteristics of electromagnetic wave propagation in underground coal seams. They verified the sensitivity of phase data to the dielectric constant and proposed a full-waveform inversion algorithm that effectively reduced the sensitivity of the inversion method to noise. Xiao et al. [21] deduced the effective penetration distance of the working face of an underground mine based on the initial field strength, receiving and transmitting distances, and field-strength attenuation coefficient. They found that only the abnormal areas with significant differences in electrical parameters were detected at frequencies below 1 MHz; however, abnormal areas with even minor differences were detected at higher frequencies [22]. Wu et al. [23] focused on the thin coal area of a working face in the Zhangji coal mine. They performed fine detection of multifrequency radio waves below 1 MHz and observed that as the working frequency increased, the field strength of the electromagnetic wave decreased while the attenuation value of the coal and rock mass increased. Korpisalo and Heikkinen [24] performed radio wave penetration to detect and interpret the shape of low-resistivity underground areas and revealed that these areas exhibited significant differences in resistivity than the

Manuscript received 9 October 2023; accepted 14 November 2023. Date of publication 20 November 2023; date of current version 4 December 2023. This work was supported by the National Key R&D Program of China under Grant 2018YFC0807805. *(Corresponding author: Yanqing Wu.)*

Shun Yang, Yanqing Wu, and Peng Lu are with the State Key Laboratory of Coal Mine Disaster Dynamics and Control, School of Resources and Safety Engineering, Chongqing University, Chongqing 400044, China (e-mail: yangshun0820@163.com; wuyanqing9@163.com; 552437915@qq.com).

Zhifang Liu is with the Institute of Intelligent Manufacturing, Chongqing Vocational College of Light Industry, Chongqing 400065, China (e-mail: liuzhifang164@163.com).

Digital Object Identifier 10.1109/JSTARS.2023.3334201

intact bedrock and fractured rock masses such as water-bearing fractures and sulfides. Their findings provided clearer and more detailed information about abnormal areas compared to other studies.

The radio-wave field strength attenuation increases in rock layers at higher frequencies and the receiving signal is unstable; therefore, the frequency of RIM is traditionally 0.1–1 MHz, and fine detection at high frequencies (above 1 MHz) has been scarcely reported. The RIM is widely used in practical implementation projects for rough predict the geologically hazardous locations. However, forward modeling and theoretical research are lacking for the RIM. Forward modeling is the foundation of the tomographic inversion method and enhances the detection precision; however, this method has not been used to determine the accuracy of the detected geologically hazardous locations in coal seams. In this study, a new high-frequency (1–8 MHz) RIM is proposed for the fine detection of far-field (100 m) electromagnetic radiation in coal seams. A reliable forward model is established based on the propagation characteristics of electromagnetic waves in lossy media and the functional relation between the electrical parameters of coal and the frequency of electromagnetic waves. Numerical simulations are conducted using a frame antenna at high frequencies, and the field strength of electromagnetic waves in coal seams with and without geological abnormal areas are compared. The field strength attenuation coefficient, wavelength, and far-field radiation characteristics of the frame antenna are used to discuss if the detected geologically hazardous location is accurate. The feasibility of high-frequency detection is further supported by the electromagnetic wave signal strength in the receiving tunnel.

II. Propagation of Electromagnetic Waves in Lossy Media

When electromagnetic waves propagate underground, coal seams, rock layers, and geological abnormal areas can be classified as lossy media. The electromagnetic wave equation for lossy media was derived based on Maxwell's equations. The Maxwell's equations for the time-harmonic field can be expressed as follows [25]:

$$\begin{cases} \nabla \times \widetilde{\mathbf{H}} = \mathrm{j}\omega\varepsilon_c\widetilde{\mathbf{E}}(1.1) \\ \nabla \times \widetilde{\mathbf{E}} = -\mathrm{j}\omega\mu\widetilde{\mathbf{H}}(1.2) \\ \nabla \cdot \widetilde{\mathbf{E}} = 0(1.3) \\ \nabla \cdot \widetilde{\mathbf{H}} = 0(1.4) \end{cases} \tag{1}$$

where $\widetilde{\mathbf{H}}$ is the magnetic field strength vector of a time-harmonic field, $\widetilde{\mathbf{E}}$ is the electric field strength vector of a time-harmonic field, ω is the electromagnetic wave angular frequency, μ is the magnetic permeability, ε_c is the complex permittivity, and j is an imaginary unit. In equation 1.1

$$\varepsilon_{\mathrm{c}} = \varepsilon - \mathrm{j}\frac{\sigma}{\omega} = \varepsilon' - \mathrm{j}\varepsilon'' \tag{2}$$

where ε is the dielectric constant of the medium, σ is the conductivity of the medium, ε' is the real part of the permittivity, and ε'' is the imaginary part of the dielectric constant.

By applying the curl operator to (1.2) and substituting (1.1) into the result, we obtain

$$\nabla \times (\nabla \times \widetilde{\mathbf{E}}) = -j\omega\mu\left(j\omega\varepsilon_c\widetilde{\mathbf{E}}\right) = \omega^2\mu\varepsilon_c\widetilde{\mathbf{E}}. \tag{3}$$

According to the vector triple product, the Laplace operator and (1.3), we can derive the following equation:

$$\nabla \times (\nabla \times \widetilde{\mathbf{E}}) = \nabla(\nabla \cdot \widetilde{\mathbf{E}}) - \nabla^2\widetilde{\mathbf{E}} = 0 - \nabla^2\widetilde{\mathbf{E}} = \omega^2\mu\varepsilon_c\widetilde{\mathbf{E}}. \tag{4}$$

The homogeneous wave equation of the time-harmonic electric field strength vector is derived from (3) and (4)

$$\nabla^2\widetilde{\mathbf{E}} + \omega^2\mu\varepsilon_c\widetilde{\mathbf{E}} = 0. \tag{5}$$

By referring to (4), we can derive the following equation based on the definitions of relative permittivity (ε_r) and relative permeability (μ_r):

$$\nabla \times (\mu_r^{-1}\nabla \times \widetilde{\mathbf{E}}) = \omega^2\mu_0\varepsilon_c\widetilde{\mathbf{E}} = (\omega\sqrt{\mu_0\varepsilon_0})^2\varepsilon_r\widetilde{\mathbf{E}} = k_0^2\varepsilon_r\widetilde{\mathbf{E}} \tag{6}$$

where $k_0 = \omega\sqrt{\mu_0\varepsilon_0} = \frac{\omega}{c_0}$, in which c_0 is the speed of light in vacuum, μ_0 is the permeability in vacuum, and ε_0 is the dielectric constant in vacuum.

The complex form of relative permittivity can be obtained from (2), $\varepsilon_{rc} = \varepsilon_r - \frac{\mathrm{j}\sigma}{\omega\varepsilon_0}$. Furthermore, by substituting (6), we can derive the wave equation for electromagnetic wave propagation in lossy media as follows:

$$\nabla \times (\mu_r^{-1}\nabla \times \widetilde{\mathbf{E}}) - k_0^2\left(\varepsilon_r - \frac{\mathrm{j}\sigma}{\omega\varepsilon_0}\right)\widetilde{\mathbf{E}} = 0. \tag{7}$$

The propagation characteristics of electromagnetic waves in a medium primarily depend on the frequency, magnetic permeability, permittivity, and conductivity. The magnetic permeability of coal seams only changes slightly; regardless, its relative magnetic permeability can be approximated as 1. The conductivity and permittivity of the propagation medium are the main considerations of this study [26].

Frame antennas are used for the geophysical exploration of the working faces of underground mines owing to the advantages such as convenience, speed, and improved radiation effectiveness. Herein, a forward model of the RIM in coal seams is established using the FEM to iteratively solve (7). To verify the accuracy of the numerical simulation, the same model was employed in the numerical simulation, theoretical solution, and field experimental, and the frame antenna is used as the transmitting antenna, the validation model as shown in Fig. 1(a). The field strength curves observed in the receiving line obtained from the numerical simulation are compared with the curve from the theoretical solution and field experimental data. The theoretical curve and field experimental data are [14] depicted in Fig. 1(b), showing good consistency.

III. Model Electrical Parameters

The detection transmitter used in the underground mines operates within the radio frequency band. The electrical conductivity and relative permittivity of coal at 1–10 MHz were measured using the TH2839 precision impedance analyzer (see Fig. 2).

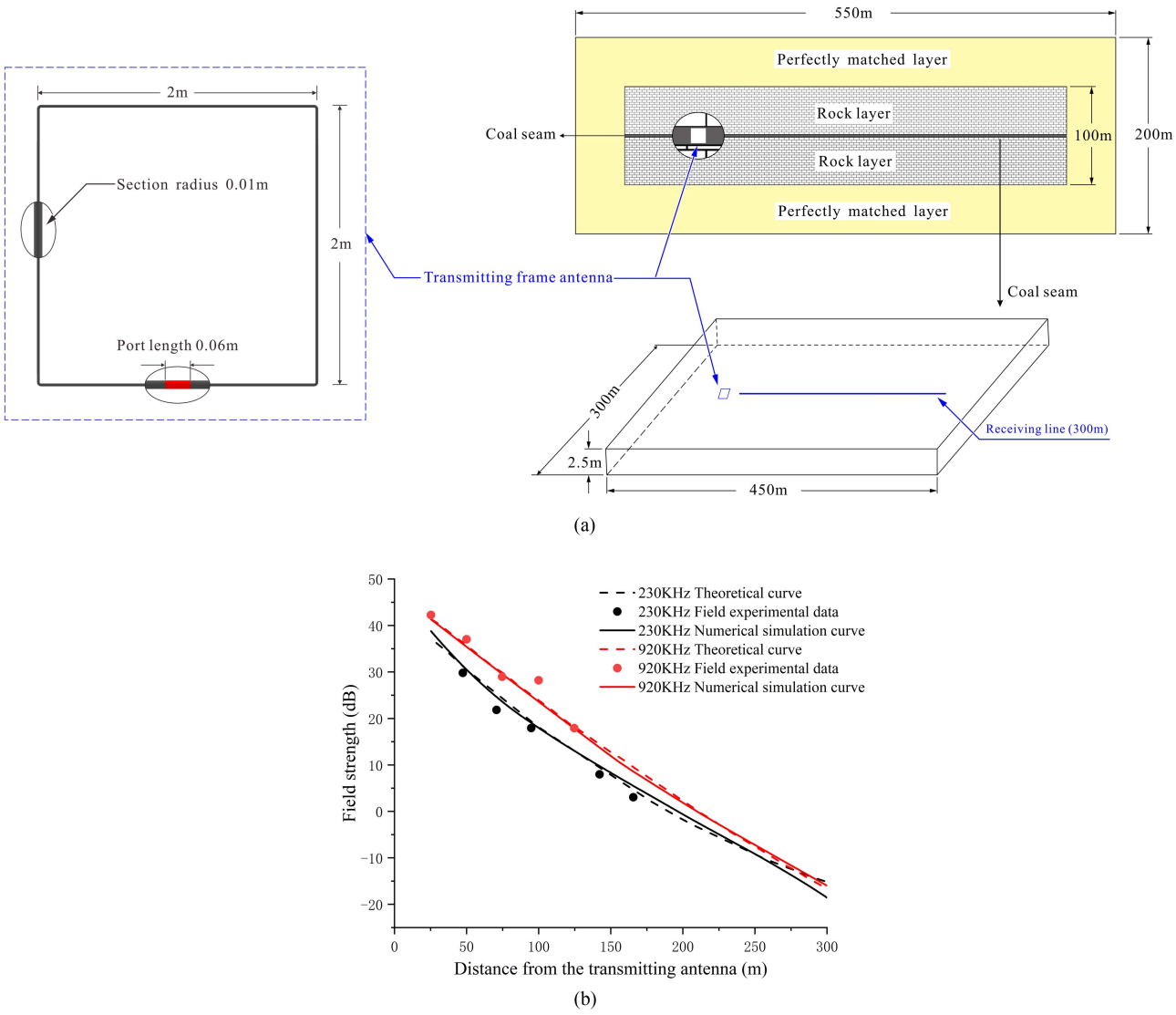

Fig. 1. (a) Schematic of the comparison model. (b) Comparison of simulation data.

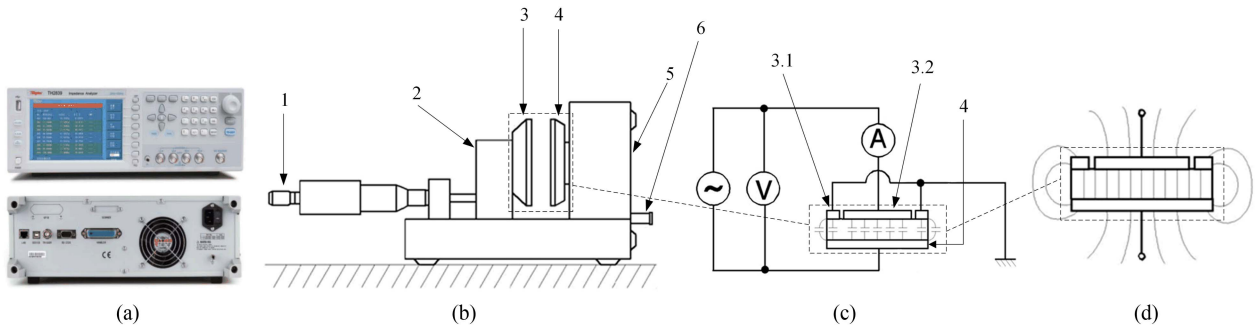

1- Micrometer small knob; 2- Fixing screw of electrode A; 3- Shielded electrode A; 3.1- Shielding end of electrode A; 3.2- Center electrode of electrode A; 4- Unshielded electrode B; 5- Screw for controlling electrode B; 6- Pressure spring of electrode A

Fig. 2. (a) TH2839 precision impedance analyzer. (b) Schematic of the electrical parameter testing fixture. (c) Schematic of testing principles. (d) Schematic of the magnetic field testing.

The TH2839 precision impedance analyzer was constructed using the auto-balancing bridge method and can be used for high-power tests. It uses the sine wave as the test signal and offers a test frequency range of 20 Hz–10 MHz, with a frequency accuracy of 0.01% and a minimum resolution of 0.01 Hz. It can also measure the impedance up to 1 GΩ, which satisfies the testing requirements.

The conductivity of coal can be determined based on the parameters measured by the analyzer as follows:

$$\sigma = \frac{1}{\rho} \tag{8}$$

$$\rho = |Z| \cos\theta \frac{S}{L} = R\frac{S}{L} \tag{9}$$

where σ is the electrical conductivity (S/m), ρ is the resistivity ($\Omega \cdot$m), $|Z|$ is the absolute value of impedance (Ω), θ is the phase angle (°), S is the cross-sectional area (m^2), L is the thickness (m), and R is the resistance (Ω).

The relative permittivity of coal can be calculated as follows:

$$\varepsilon_r = \frac{t_a \times C_p}{A \times \varepsilon_0} = \frac{t_a \times C_p}{\pi \times \left(\frac{d}{2}\right)^2 \times \varepsilon_0} \tag{10}$$

where C_P is the equivalent parallel capacitance (F), t_a is the average thickness (m) of the tested material, A is the area (m^2) of the testing electrode in the shielding electrode, and d is the diameter (m) of the testing electrode in the shielding electrode.

A. Relationship Between Coal Electrical Parameters and Frequency

The electrical conductivity and relative permittivity of coal, rock, and geological abnormal areas within the model exhibit frequency-dependent changes. Thus, the model parameters must be accurately determined. To this end, the electrical parameters were obtained at different frequencies using the TH2839 precision impedance analyzer and relevant literature [27], [28], [29], [30], [31], [32], [33], [34], [35]. Then, the functions describing the relation between the conductivity and permittivity of coal and frequency were fitted and summarized, as shown in Fig. 3. Results showed that the conductivity and permittivity of coal varied with frequency.

As shown in Fig. 3(a), the electrical conductivity of coal has a positive exponential relation with frequency. The conductivity gradually increases with frequency. The corresponding fitting function is as follows:

$$\sigma = 1.77 \times 10^{-4} e^{5.02\times10^{-7} * f} - 1.2 \times 10^{-4}. \tag{11}$$

The fitting coefficient R^2 for the given relationship is 99.63%. When the frequency is 1 MHz, the conductivity is 1.724 $\times$ 10^{-4} S/m, which aligns with field observations. This value of conductivity can serve as the basis for parameter selection for forward modeling.

Fig. 3(b) shows that the relative permittivity of coal has a negative exponential relation with frequency. The relative permittivity gradually decreases with increasing frequency. At higher frequencies, the relative permittivity tends to stabilize. The corresponding fitting function is as follows:

$$\varepsilon_r = 1.69 + 2.34 e^{-0.52 * \log(f)}. \tag{12}$$

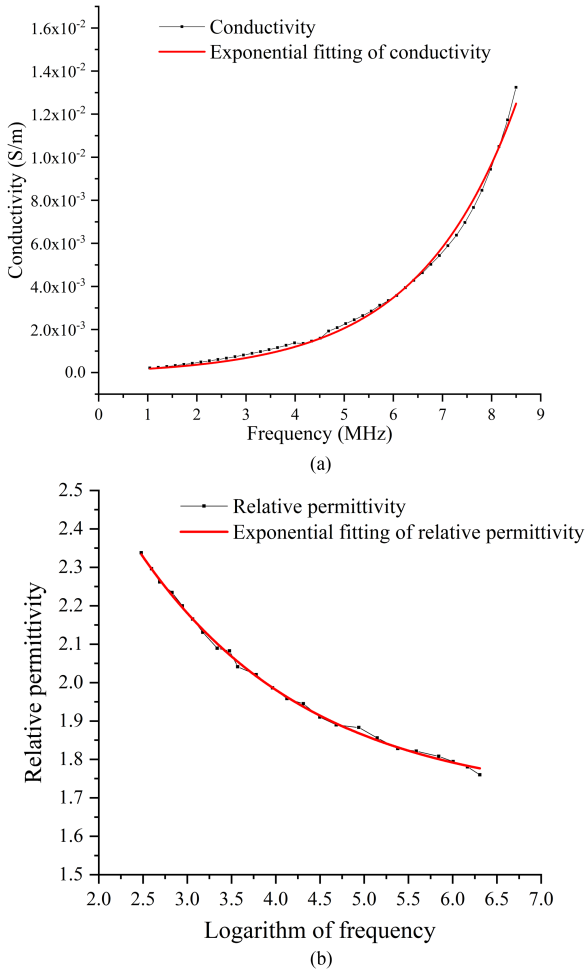

Fig. 3. Fitting curve of the electricity parameters of coal and test frequency. (a) Conductivity [27]. (b) Relative permittivity [28].

B. Electrical Parameters of Rock layer, Geological Abnormal Area, and Boundary

Based on the ranges of conductivity and relative permittivity of sandstone and mudstone [36] and [37], we assumed that the changes in the conductivity and relative permittivity of the rock layer with frequency follow a similar pattern to that of the electrical parameters of coal. The conductivity and relative permittivity of the rock layer were 30 times and 6 units higher than those of coal. Geological abnormal areas often contain water-conducting channels and water-rich regions, leading to higher conductivity and relative permittivity. Thus, the conductivity and relative permittivity of those areas were considered to be 1.75 $\times$ 10^4 times and 38 units higher than that of coal.

Table I presents the conductivity and relative permittivity of coal, rock layer, and abnormal areas at a frequency of 1 MHz.

IV. Model Overview and Boundary Conditions

A. Model Overview

The simulation model adopts a space domain of 600 m $\times$ 600 m $\times$ 600 m. To mitigate reflection and error caused by the truncated boundary, a perfectly matched layer (PML) was

TABLE I
ELECTROMAGNETIC PARAMETERS OF EACH LAYER AT A FREQUENCY OF 1 MHZ

Conductivity of coal (S/m)	Relative permittivity of coal	Conductivity of rock layer (S/m)	Relative permittivity of rock layer	Conductivity of abnormal area (S/m)	Relative permittivity of abnormal area
1.72×10^{-4}	1.69	5.16×10^{-3}	7.69	3.01	39.69

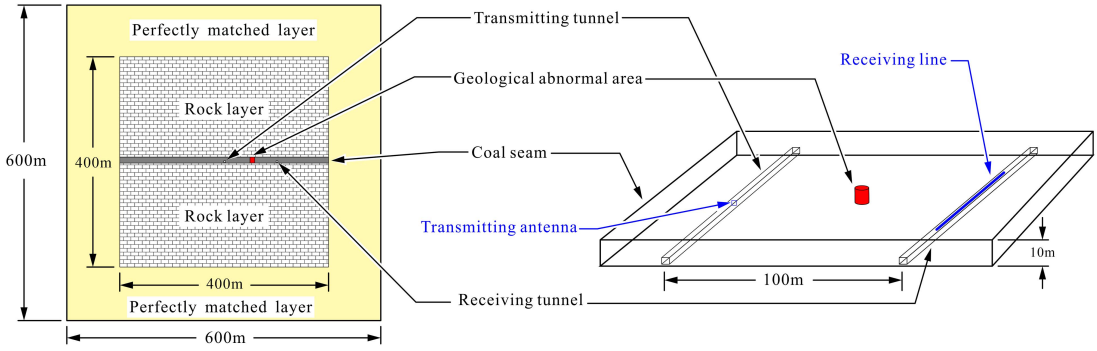

Fig. 4. Model overview and detection layout.

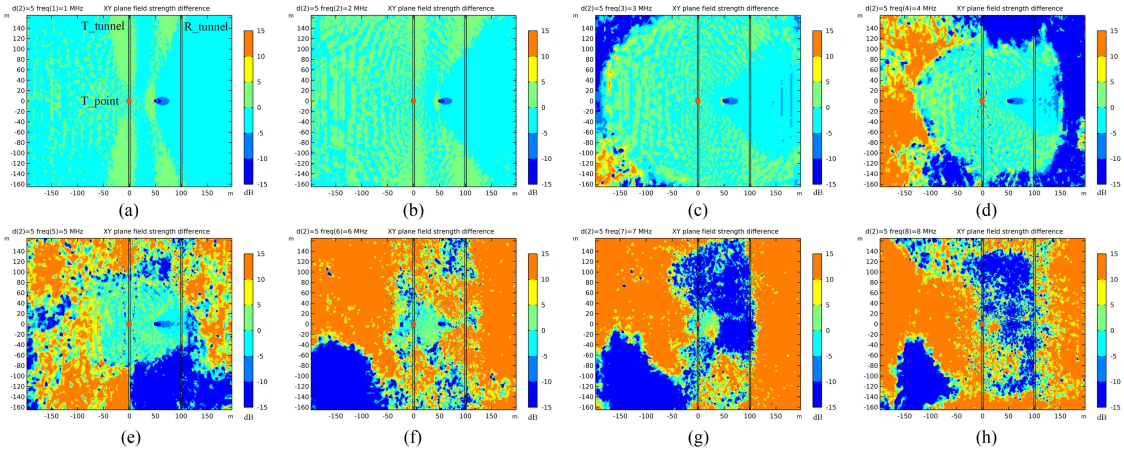

Fig. 5. Maps of the differences in field strength for the collapse column of 5-m diameter with different frequencies. (a) 1 MHz. (b) 2 MHz. (c) 3 MHz. (d) 4 MHz. (e) 5 MHz. (f) 6 MHz. (g) 7 MHz. (h) 8 MHz.

implemented to absorb incident waves. The thickness of the PML was set as 100 m. In addition, an interlayer was included at the center of the model to simulate the coal seam. The coal seam was 10 m thick, and the working face was 100 m wide and 400 m long. To enhance the realism of the underground mine, transmitting and receiving tunnels of 400 m × 3 m × 2.5 m were established. In the middle of these tunnels, a cylindrical structure was simulated as a collapsed column that resembled a geological abnormal area within the coal seam. The transmitting antenna, positioned in the middle of the transmitting tunnel, was aligned in a straight line with the collapsed column, as shown in Fig. 4.

For high-frequency detection of anomalies, several studies compared the transmitting frequency and the size of the geological abnormal area. Herein, the transmitting frequencies were selected as 1.0, 2.0, 3.0, 4.0, 5.0, 6.0, 7.0, and 8.0. The diameters

TABLE II
ELECTROMAGNETIC PARAMETERS OF THE TRANSITION BOUNDARY AT 1 MHZ

Conductivity of the abnormal area boundary (S/m)	Relative permittivity of the abnormal area boundary	Skin depth of the abnormal area boundary (m)
8.62×10^{-3}	39.69	5.42

TABLE III
SKIN DEPTH OF THE ABNORMAL AREA BOUNDARY WITH HIGH FREQUENCIES

Frequency (MHz)	1	2	3	4	5	6	7	8
Skin depth of the abnormal area (m)	5.42	2.64	1.58	1.03	0.70	0.49	0.35	0.26

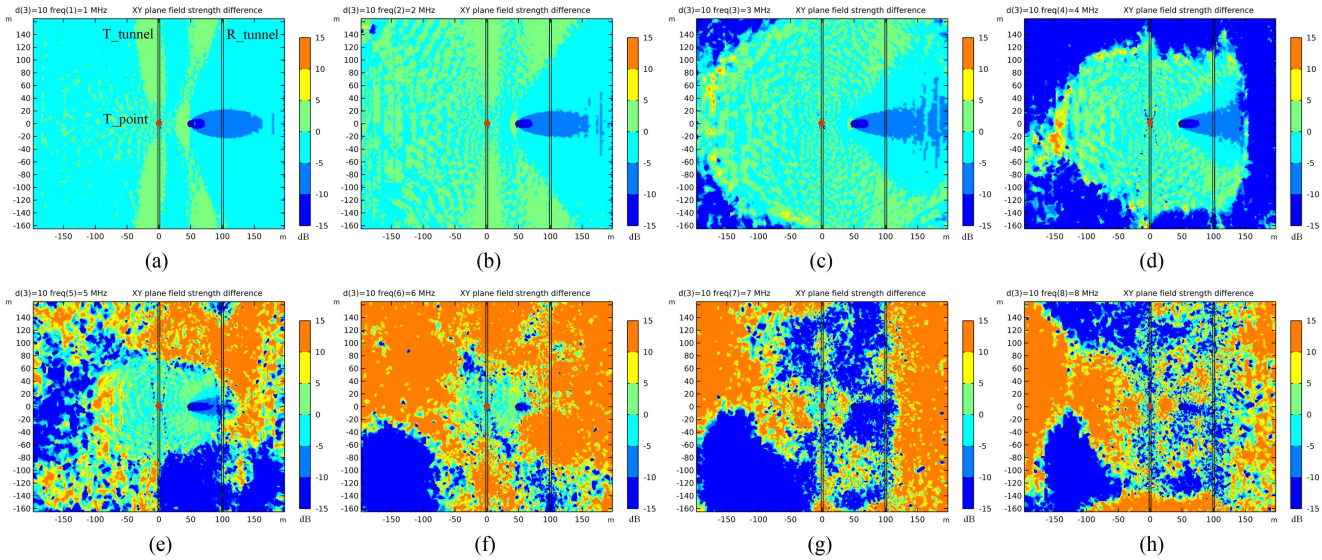

Fig. 6. Maps of the differences in field strength for the collapse column of 10-m diameter with different frequencies. (a) 1 MHz. (b) 2 MHz. (c) 3 MHz. (d) 4 MHz. (e) 5 MHz. (f) 6 MHz. (g) 7 MHz. (h) 8 MHz.

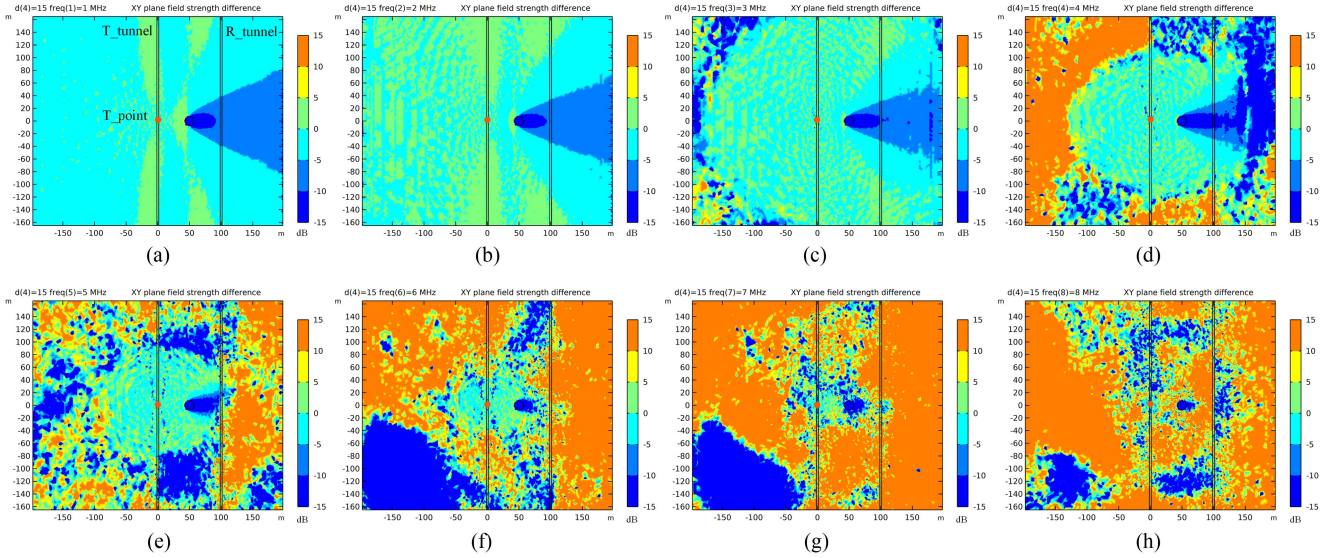

Fig. 7. Maps of the differences in field strength for the collapse column of 15-m diameter with different frequencies. (a) 1 MHz. (b) 2 MHz. (c) 3 MHz. (d) 4 MHz. (e) 5 MHz. (f) 6 MHz. (g) 7 MHz. (h) 8 MHz.

of the collapse columns in the geological abnormal areas were set as 5, 10, 15, and 30, respectively.

B. Boundary Conditions

The transition boundary between coal and the geological abnormal area is crucial for numerical simulation. When the electromagnetic waves cross this boundary, it results in an energy loss. Thus, a transition boundary condition is introduced. The total impedance of the electromagnetic wave passing through the boundary is calculated based on the thickness of the boundary and the tangential impedance. The material properties and boundary thickness are used as the input parameters for the transition boundary condition.

Table II presents the electromagnetic parameters of the transition boundary used for accurately modeling the energy loss during wave crossing. The thickness of the transition boundary is set to the skin depth at the respective frequency. The skin depth varies with each frequency, as shown in Table III, which is used in high-frequency simulation.

By incorporating the transition boundary condition and accurately defining the material properties and thickness of the boundary, the energy loss is determined via simulation and the surface currents on both sides of the boundary are calculated. This approach enhances the realism of the numerical model and

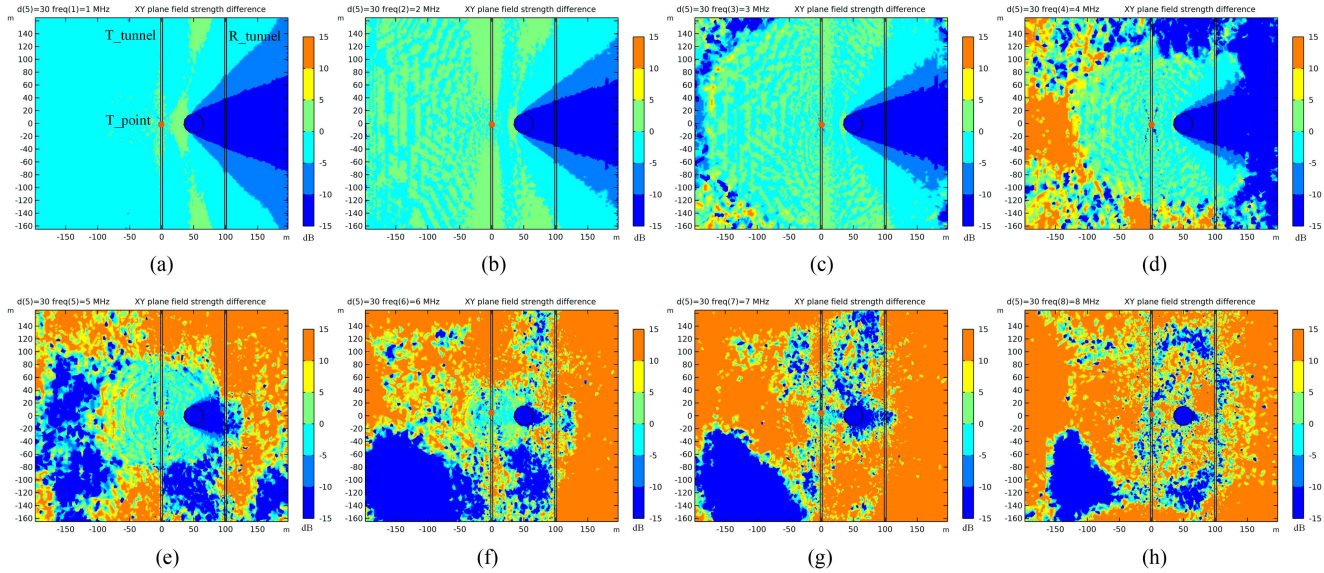

Fig. 8. Maps of the differences in field strength for the collapse column of 30-m diameter with different frequencies. (a) 1 MHz. (b) 2 MHz. (c) 3 MHz. (d) 4 MHz. (e) 5 MHz. (f) 6 MHz. (g) 7 MHz. (h) 8 MHz.

TABLE IV
ELECTROMAGNETIC WAVE PROPAGATION CHARACTERISTICS IN DIFFERENT LOSS MEDIA

	General Media $(0.01<\frac{\sigma}{\omega\varepsilon}<100)$	Lossless media $(\sigma=0)$	Low-loss media $(\frac{\sigma}{\omega\varepsilon}<0.01)$	Good conductor $(\frac{\sigma}{\omega\varepsilon}>100)$	Unit
α	$\omega\left[\frac{\mu\varepsilon}{2}\left[\sqrt{1+\left(\frac{\sigma}{\omega\varepsilon}\right)^2}-1\right]\right]^{1/2}$	0	$\frac{\sigma}{2}\sqrt{\frac{\mu}{\varepsilon}}$	$\sqrt{\pi f\mu\sigma}$	(Np/m)
β	$\omega\left[\frac{\mu\varepsilon}{2}\left[\sqrt{1+\left(\frac{\sigma}{\omega\varepsilon}\right)^2}+1\right]\right]^{1/2}$	$\omega\sqrt{\mu\varepsilon}$	$\omega\sqrt{\mu\varepsilon}$	$\sqrt{\pi f\mu\sigma}$	(rad/m)
μ_p	ω/β	$1/\sqrt{\mu\varepsilon}$	$1/\sqrt{\mu\varepsilon}$	$\sqrt{4\pi f/\mu\sigma}$	(m/s)
λ	$2\pi/\beta=u_p/f$	u_p/f	u_p/f	u_p/f	(m)

provides valuable insights into the behavior of electromagnetic waves when passing through transition boundaries between different geological areas.

V. ANALYSIS OF SIMULATION RESULTS

Herein, the field strengths of electromagnetic waves in coal seams with and without the geological abnormal area are compared. Forward modeling was performed without the geological abnormal area, and the results are shown in the field strength distribution diagram H_1. Then, the geological abnormal area was incorporated into the model, and forward simulation was performed; the results are shown in the field strength distribution diagram H_2. Finally, the difference in field strength ($\Delta H = 20 \times \log 10(H_2 - H_1)$) was calculated.

A. Forward Modeling of the Fine Detection of High-Frequency Electromagnetic Waves

1) Collapse Column of 5-m Diameter: T_tunnel is the Transmitting tunnel, R_tunnel is the Receiving tunnel, T_point is the location of transmitting antenna.

2) Collapse Column With 10-m Diameter: T_tunnel is the Transmitting tunnel, R_tunnel is the Receiving tunnel, T_point is the location of transmitting antenna.

3) Collapse Column With 15-m Diameter: T_tunnel is the Transmitting tunnel, R_tunnel is the Receiving tunnel, T_point is the location of transmitting antenna.

4) Collapse Column With 30-m Diameter: T_tunnel is the Transmitting tunnel, R_tunnel is the Receiving tunnel, T_point is the location of transmitting antenna.

As shown in Figs. 5–8, the electromagnetic wave generates a distinct "shadow area" behind the collapse column. The size and

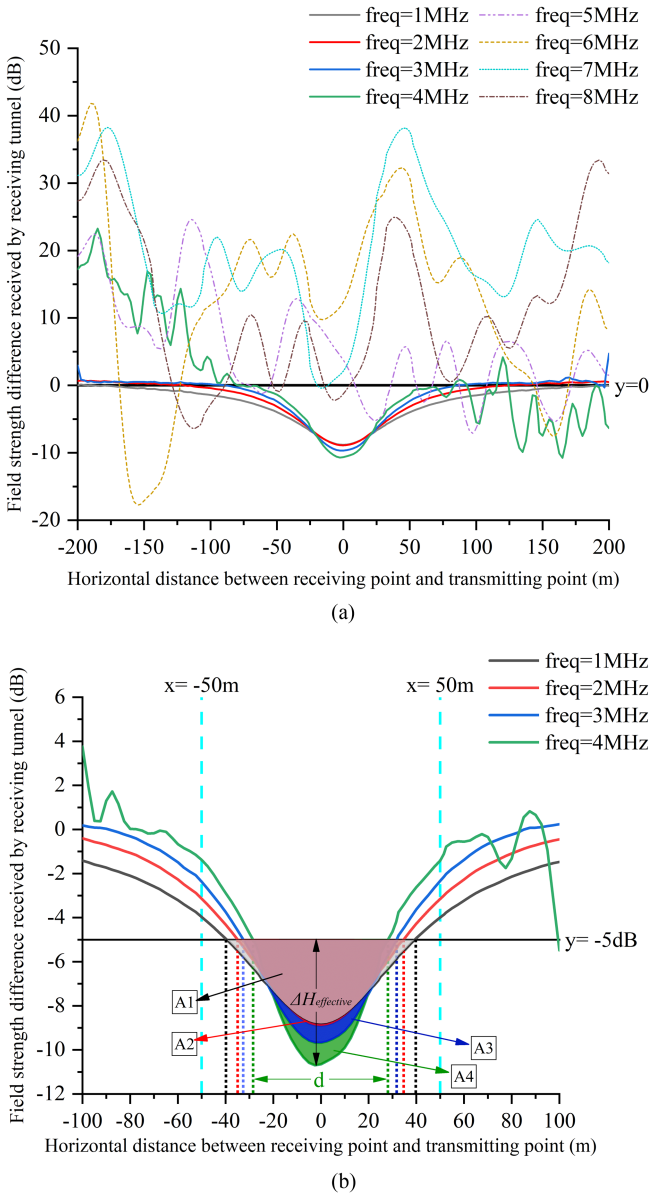

Fig. 9. High-frequency detection of electromagnetic wave signals received by the receiving tunnel. (a) Field strength difference. (b) Effective geological abnormal area.

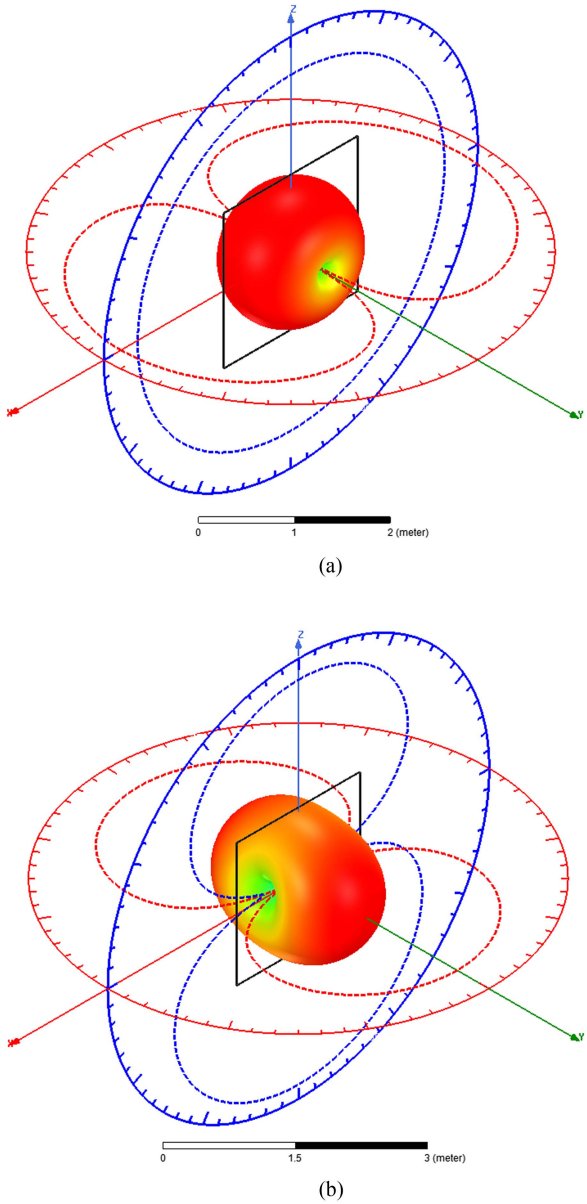

Fig. 10. Typical far-field radiation patterns. (a) Electrically small loop (electric length is 0.01). (b) Electrically large loop (electric length is 1).

extent of this "shadow area" are influenced by the frequency of the electromagnetic wave and the dimensions of the collapse column. To quantitatively analyze the characteristics of the "shadow area" and its impact on the detection of anomalies, the field strengths of the electromagnetic waves from the receiving tunnel were recorded. The effective geological abnormal area is defined as the region where the field strength attenuation is 5 dB or greater (indicated by blue and dark blue areas in Figs. 5–8). The detection accuracy is determined by analyzing the extent of the effective geological abnormal area.

For the 5-m-diameter collapse column, the field strength attenuation received by the receiving tunnel was <5 dB across the frequency range of 1–8 MHz. Thus, identifying the geological abnormal area associated with this collapse column was challenging. For the 10-m-diameter collapse column, the geological abnormal area could be detected within the frequency range of 1–4 MHz. As the frequency increased, the "shadow area" gradually shrunk, leading to a more precise localization of the collapse column. However, when the frequency exceeded 4 MHz, the "shadow area" reduced to an extent that the receiving tunnel no longer captured the effective geological abnormal area; thus, the collapse column could not be detected. Hence, the highest detection accuracy is achieved at 4 MHz detection frequency in this condition.

For 15-m- and 30-m-diameter collapse columns, the "shadow area" was larger compared to that for the 5-m- and 10-m-diameter collapse columns. The "shallow area" reduces in size as the frequency increases. To assess the effect of fine detection

more comprehensively, data recorded at high frequencies for the 15-m-diameter collapse column were extracted and analyzed; the results are shown in Fig. 9.

As shown in Fig. 9(a), for the frequency range of 1–4 MHz, the field strength difference measured in the receiving tunnel exhibits a noticeable attenuation range (with field strength difference below 0) around the geological abnormal area. As the frequency increases, the attenuation range gradually decreases, indicating an improvement in the detection accuracy. However, as the frequency continuously increases (5–8 MHz), the receiving tunnel fails to accurately receive the electromagnetic wave signal, resulting in distorted signals that do not follow a discernible pattern. This suggests that as the frequency increases, the attenuation of electromagnetic wave propagation in the coal seams becomes more prominent, leading to shorter propagation distances.

The field strength difference measured in the receiving tunnel within the range above 5 dB is defined as the effective detection range ["d" in Fig. 9(b)]. Effective detection value ["ΔHeffective" in Fig. 9(b)] is obtained by subtracting 5 dB from the absolute attenuation value. The effective detection ranges for frequencies of 1, 2, 3, and 4 MHz are 79.53, 69.63, 64.39, and 56.68 m, respectively. This indicates that as the frequency increases, the effective detection range decreases, leading to a 28.73% increase in accuracy and more precise determination of the location of the collapse column. Moreover, the attenuation of electromagnetic waves gradually increases, measuring 3.83, 3.91, 4.68, and 5.76 dB at the frequencies of 1, 2, 3, and 4 MHz, respectively. This shows that as the frequency increases in the range of 1–4 MHz, the attenuation of electromagnetic waves in the coal seam and collapse column intensifies. In Fig. 9(b), A1, A2, A3, and A4 represent the effective detection areas at frequencies of 1, 2, 3, and 4 MHz, respectively. It clearly illustrates that as the frequency increases in the range of 1–4 MHz, the accuracy of detecting the geological abnormal area improves.

VI. Discussion

Based on the characteristics of electromagnetic wave propagation in lossy media, formulas for calculating the field strength attenuation coefficient (α), phase constant (β), phase velocity (μ_p), and wavelength (λ) in different types of media have been derived [25], [38] and presented in Table IV.

In the frequency range of 1–8 MHz, the coal seam and rock layers are classified as general media, whereas the geological abnormal area is considered a good conductor. Using the fitted functions of conductivity and permittivity shown in Section III, we calculated the field strength attenuation coefficient and wavelength of electromagnetic waves propagating in the coal seam, rock layer, and geological abnormal area at different frequencies. The results are summarized in Tables V and VI.

Table V shows the variations in field strength attenuation coefficients across different media, which are influenced by the frequency and electrical parameters of the propagation medium. At the same frequency, the attenuation of electromagnetic waves in the rock layers and geological abnormal area is more pronounced compared to that in the coal seam. In addition, the field strength attenuation becomes more intensified as the frequency increases across all three media.

TABLE V
Field Strength Attenuation Coefficients in Different Media at Frequencies of 1–8 MHz

Frequency (MHz)	Coal seam (Np/m)	Rock layer (Np/m)	Geological abnormal area (Np/m)
1.0	0.02	0.14	3.45
2.0	0.04	0.28	7.08
3.0	0.07	0.48	11.85
4.0	0.12	0.74	18.19
5.0	0.18	1.09	26.66
6.0	0.26	1.55	37.97
7.0	0.38	2.18	53.07
8.0	0.53	3.01	73.22

TABLE VI
Electromagnetic Wavelength in Different Media at Frequencies of 1–8 MHz

Frequency (MHz)	Coal seam (m)	Rock layer (m)	Geological abnormal area (m)
1.0	185.52	42.19	1.82
2.0	91.51	20.60	0.89
3.0	57.26	12.40	0.53
4.0	39.14	8.14	0.35
5.0	27.84	5.59	0.24
6.0	20.19	3.95	0.17
7.0	14.80	2.84	0.12
8.0	10.92	2.06	0.086

Table VI shows that electromagnetic wavelength considerably varies across different media. It is influenced by the frequency and electrical parameters of the propagation medium. In particular, the wavelength is relatively longer in the coal seam and shorter in the rock layer and geological abnormal area. Furthermore, as the frequency increases, the wavelength decreases in all three mediums.

Based on the attenuation coefficient and wavelength in different media, the following observations can be made within the frequency range of 1–8 MHz. At low frequencies, the field strength attenuation coefficients are relatively low and the electromagnetic waves exhibit long wavelengths in the coal seam. When encountering a geological abnormal area, they undergo diffraction, which causes the waves to take a shorter propagation path through the geological abnormal area and results in smaller attenuation amplitudes of the electromagnetic wave signal. Conversely, at high frequencies, the field strength attenuation coefficients are relatively higher and the electromagnetic wavelength in the coal seam becomes shorter. When encountering a geological abnormal area, they undergo transmission, which causes significant signal attenuation in the receiving tunnel. In addition, the reflection from the geological abnormal area becomes more pronounced due to the shorter wavelength and increased field strength attenuation.

TABLE VII
ELECTRICAL LENGTHS OF FRAME ANTENNA WITH DIFFERENT FREQUENCIES IN COAL SEAMS

Frequency (MHz)	1	2	3	4	5	6	7	8
Frame antenna electrical length (m)	0.043	0.087	0.140	0.204	0.287	0.396	0.540	0.733

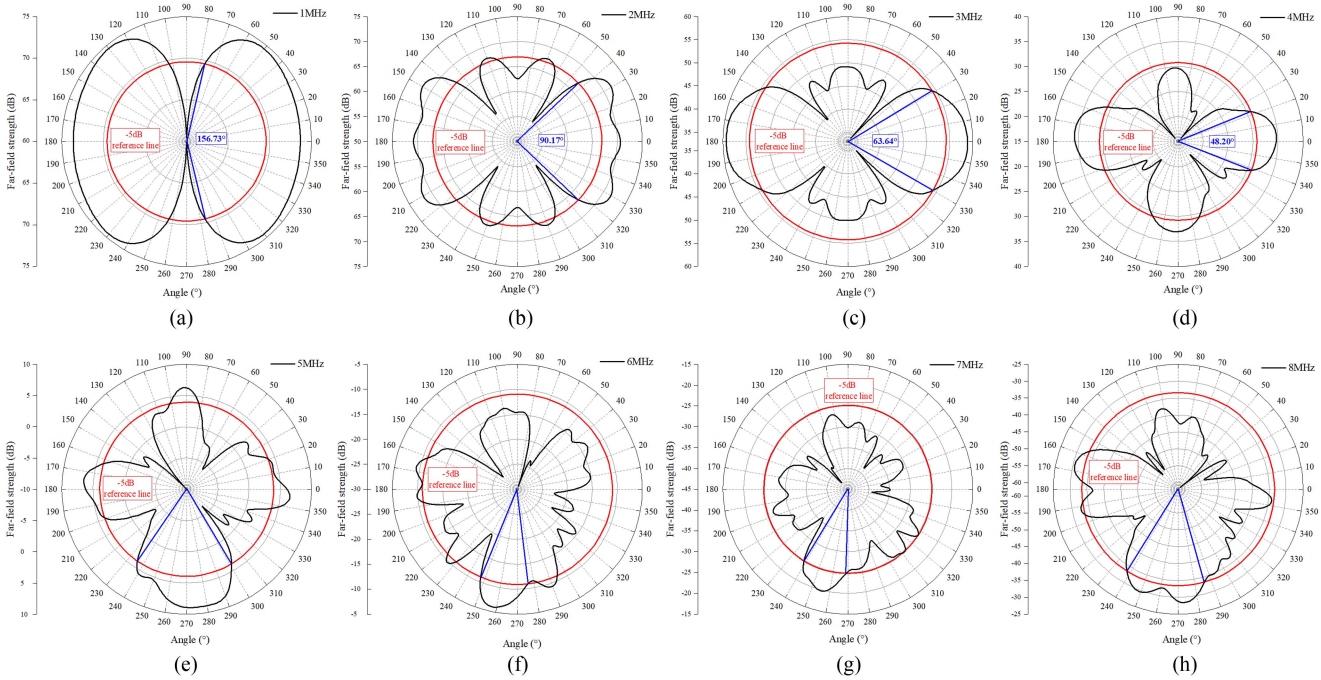

Fig. 11. Far-field radiation patterns of the frame antenna for the high-frequency detection of electromagnetic waves.

Currently, the frame antenna is predominantly employed for underground radio wave detection. The far-field radiation direction of the frame antenna is determined by its electric length, which can be calculated as the ratio of the circumference of the frame antenna (C) to the electromagnetic wavelength (λ). The calculated electrical lengths of the frame antenna at different frequencies in coal seams are shown in Table VII. The circumference of the frame antenna used herein is 8 cm.

When the electric length of the frame antenna is <0.1, the underground antenna has an electrically small-loop radiation. In this case, the far-field pattern remains the same, as shown in Fig. 10(a). When the electric length is 0.01, the far-field radiation pattern of the frame antenna is omnidirectional on the torus and exhibits an eight-shaped pattern at the cross section. The radiation direction of the underground frame antenna varies with changes in frequency and electrical parameters of the propagation medium, resulting in a shift in the electric length of the frame antenna. Fig. 10(b) shows that when the electrical length is 1, the frame antenna displays an eight-shaped pattern on the torus and cross section. The maximum radiation direction is perpendicular to the torus, exhibiting the characteristics of an electrically large-loop radiation [39], [40].

During the fine detection of high-frequency electromagnetic waves using frame antennas in the working faces of underground coal mines, it was observed that the changes in the transmitting frequency and electrical parameters of the propagation medium influenced the far-field radiation direction of the frame antenna. Fig. 11 illustrates this effect, where the red and blue lines represent the reference line and lobe width of -5 dB field strength attenuation, respectively.

The results shown in Fig. 11 indicate that as the frequency increases from 1 to 4 MHz, the lobe width of the -5 dB field strength attenuation decreases from 156.73° to 48.20° and the far-field radiation direction of the antenna becomes more focused; this results in a narrower radiation range and improved signal quality. This concentration of the receiving signal in the receiving tunnel facilitates a more accurate reflection of geological abnormal areas. It also explains the phenomenon of the "shadow area" narrowing behind the collapse column, as observed in Figs. 5–8. However, when the frequency ranges from 5 to 8MHz, the direction of far-field maximum radiation of the frame antenna changes, leading to poorer signal quality. Thus, the receiving tunnel cannot capture strong signals, which reduces the detection efficiency, and the geological abnormal area is not accurately reflected.

Fig. 12 shows the far-field radiation pattern of the frame antenna at 100 m with frequencies of 1–8 MHz. The corresponding maximum field strength values observed in the receiving tunnel are 74.56, 71.91, 59.26, 35.79, 8.95, -5.96, -19.79, and -28.42 dB, respectively. These values indicate that the far-field radiation

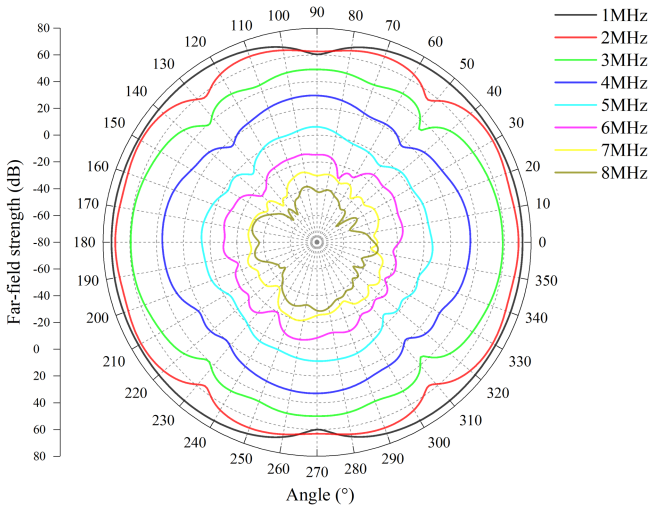

Fig. 12. Merged far-field radiation direction patterns of the frame antenna for the high-frequency detection of electromagnetic waves.

field strength decreases as the frequency increases. Notably, when the frequency is within 1–4MHz, the field strength in the receiving tunnel exceeds 30 dB. This finding underscores the feasibility of high-frequency detection in underground mines.

VII. Conclusion

The study of RIM holds significant importance in preventing geological disasters, reducing safety accidents, minimizing blind construction, and ensuring safe and efficient production in coal mines. In this study, the forward modeling for the fine detection of geological abnormal area in coal seams using a high-frequency RIM was conducted, and the conclusions are as follows.

1) By considering the propagation characteristics of electromagnetic waves in a lossy medium and the functional relation between the electrical parameters of coal, rock layers, geological abnormal areas, and the frequency of electromagnetic waves, a reliable forward model for underground high-frequency fine detection can be established using the frame antenna and FEM. Two forward numerical simulations are conducted with and without a geological abnormal area in the working face of coal mines. The map of the resulting field strength difference reveals the formation of a "shadow area" caused by the geological abnormal area.
2) The electromagnetic wave generates a noticeable "shadow area" where the field strength attenuates behind the geological abnormal area. This "shadow area" is influenced by the frequency and size of the geological abnormal area. As the detection frequency increases from 1 to 8 MHz, the "shadow area" gradually diminishes, leading to a more precise field strength attenuation area received by the receiving tunnel and higher detection accuracy. However, beyond a maximum detection frequency, the field strength attenuation cannot be achieved. Moreover, the higher the frequency, the faster the attenuation of the electromagnetic wave; thus, the receiving tunnel does not receive an effective signal.
3) The accuracy of high-frequency detection (1–8 MHz) is analyzed based on the attenuation coefficient, wavelength, and far-field radiation characteristics of the frame antenna. Low-frequency electromagnetic waves exhibit a relatively small field strength attenuation coefficient and have long wavelengths, resulting in insignificant field strength attenuation. Furthermore, the far-field radiation of the frame antenna is not concentrated, leading to a wide range of signal attenuation and low detection accuracy. Contrastingly, high-frequency electromagnetic waves have a relatively larger attenuation coefficient and shorter wavelengths, which cause significant field strength attenuation. Moreover, at high frequencies, the far-field radiation of the frame antenna becomes more concentrated, making it more sensitive to detecting geological abnormal areas. Thus, higher frequencies result in improved detection accuracy. However, as the frequency surpasses 4 MHz, the maximum far-field radiation direction of the frame antenna undergoes a change and the field strength attenuation coefficient considerably increases. Consequently, the strength of the electromagnetic wave signal decreases and the receiving tunnel does not receive the signal effectively, hindering the detection of geological abnormal areas.

In this study, the detection effect of the electromagnetic waves is quantitatively analyzed, providing a theoretical basis for the high-frequency RIM detection of geological abnormal areas. However, the degree of fracture and water content of the geological abnormal area will affect its electrical parameters, thereby affecting the imaging effect, moreover, the far distance detecting and the stability of receive signals need further research in the future.

References

[1] J. Yue, H. Zhang, H. Yang, and F. Li, "Electrical prospecting methods for advance detection: Progress, problems, and prospects in Chinese coal mines," *IEEE Geosci. Remote Sens. Mag.*, vol. 7, no. 3, pp. 94–106, Sep. 2019, doi: 10.1109/MGRS.2018.2890677.

[2] B. Su, S. Liu, L. Deng, P. Gardoni, G. M. Krolczyk, and Z. Li, "Monitoring direct current resistivity during coal mining process for underground water detection: An experimental case study," *IEEE Trans. Geosci. Remote Sens.*, vol. 60, 2022, Art. no. 5915308, doi: 10.1109/TGRS.2022.3173623.

[3] Z. Jiang, L. Liu, S. Liu, and J. Yue, "Surface-to-underground transient electromagnetic detection of water-bearing goaves," *IEEE Trans. Geosci. Remote Sens.*, vol. 57, no. 8, pp. 5303–5318, Aug. 2019, doi: 10.1109/TGRS.2019.2898904.

[4] B. Su, J. Yu, G. M. Krolczyk, P. Gardoni, and Z. Li, "Innovative surface-borehole transient electromagnetic method for sensing the coal seam roof grouting effect," *IEEE Trans. Geosci. Remote Sens.*, vol. 60, 2022, Art. no. 5702509, doi: 10.1109/TGRS.2022.3149212.

[5] H. Yuan, J. Liu, and Y. Yuan, "Using 4-D seismic data for detecting gob areas of coal mines: A case study from the Zhangji coal mine," *IEEE Trans. Geosci. Remote Sens.*, vol. 60, 2022, Art. no. 5917810, doi: 10.1109/TGRS.2022.3191676.

[6] L. Yuan, "Scientific conception of precision coal mining," *J. China Coal Soc.*, vol. 42, no. 1, pp. 1–7, 2017, doi: 10.13225/j.cnki.jccs.2016.1661.

[7] X. Lu and S. Kan, "Geological guarantee and transparent geological cloud computing technology of precision coal mining," *J. China Coal Soc.*, vol. 44, no. 8, pp. 2296–2305, 2019, doi: 10.13225/j.cnki.jccs.KJ19.0561.

[8] P. Hatherly, "Overview on the application of geophysics in coal mining," *Int. J. Coal Geol.*, vol. 114, pp. 74–84, Jul. 2013, doi: 10.1016/j.coal.2013.02.006.
[9] S. Liu, J. Liu, and J. Yue, "Development status and key problems of Chinese mining geophysical technology," *J. China Coal Soc.*, vol. 39, no. 1, pp. 19–25, 2014, doi: 10.13225/j.cnki.jccs.2013.0587.
[10] S. Liu and J. Ni, "Review for cross-hole electromagnetic method," *Prog. Geophys. Chin.*, vol. 35, no. 1, pp. 153–165, 2020, doi: 10.6038/pg2020DD0088.
[11] R. Wu, Y. Pang, and Z. Hu, "Research progress of radio wave detection technology in coal face," *Prog. Geophys. Chin.*, vol. 37, no. 5, pp. 2196–2204, 2022, doi: 10.6038/pg2022FF0480.
[12] D. A. Hill, "Radio propagation in a coal seam and the inverse problem," *J. Res. Natl. Bur. Stand.*, vol. 89, no. 5, pp. 385–394, Sep. 1984, doi: 10.6028/jres.089.022.
[13] J. R. Wait, "Radiowave propagation in a coal seam with inhomogeneous rock walls," *IEEE Trans. Geosci. Remote Sens.*, vol. 29, no. 3, pp. 469–472, May 1991, doi: 10.1109/36.79439.
[14] Y. Wu, "Underground electromagnetic wave methods and applications," Ph.D. dissertation, Central South Univ., Changsha, China, 2002.
[15] Y. Li and R. S. Smith, "Forward modeling of radio imaging (RIM) data with the Comsol RF module," *Comput. Geosci.*, vol. 85, pp. 60–67, Dec. 2015, doi: 10.1016/j.cageo.2015.08.012.
[16] Y. Li and R. S. Smith, "Modelling and straight-ray tomographic imaging studies of cross-hole radio-frequency electromagnetic data for mineral exploration: Radio-frequency EM data for mineral exploration," *Geophys. Prospect.*, vol. 66, no. 2, pp. 282–299, Feb. 2018, doi: 10.1111/1365-2478.12516.
[17] Y. Li and R. S. Smith, "Contrast source inversion (CSI) for cross-hole radio imaging (RIM) data – Part 1: Theory and synthetic studies," *J. Appl. Geophys.*, vol. 161, pp. 45–55, Feb. 2019, doi: 10.1016/j.jappgeo.2018.12.002.
[18] Y. Li and R. S. Smith, "Contrast source inversion (CSI) method to cross-hole radio-imaging (RIM) data - part 2: A complex synthetic example and a case study," *J. Appl. Geophys.*, vol. 150, pp. 93–100, Mar. 2018, doi: 10.1016/j.jappgeo.2018.01.003.
[19] Y. Li, "Forward modelling and imaging method studies for cross-hole radio imaging (RIM) data," Ph.D. dissertation, Laurentian Univ., Sudbury, Canada, 2017.
[20] L. Yue, "Study on the propagation law of electromagnetic wave in coal seam and its full waveform probabilistic inversion method," Ph.D. dissertation, China Univ. Mining Technol., Xuzhou, China, 2016.
[21] Y. Xiao, R. Wu, J. Yan, and P. Zhang, "Field strength propagation law of radio wave penetration and effective perspective width for coal face," *J. China Coal Soc.*, vol. 42, no. 3, pp. 712–718, 2017, doi: 10.13225/j.cnki.jccs.2016.0646.
[22] Y. Xiao, R. Wu, J. Yan, and P. Zhang, "Detection of multi-frequency radio wave penetration in stope face," *Coal Geol. Explor.*, vol. 44, no. 5, pp. 146–154, 2016, doi: 10.3969/j.issn.1001-1986.2016.05.028.
[23] R. Wu, G. Shen, H. Wang, and Y. Xiao, "Multi frequency perspective fine detection of radio wave for thin coal areas in fully mechanized coal face," *Coal Geol. Explor.*, vol. 48, no. 4, pp. 34–40, 2020, doi: 10.3969/j.issn.1001-1986.2020.04.005.
[24] A. Korpisalo and E. Heikkinen, "Radiowave imaging research (RIM) for determining the electrical conductivity of the rock in borehole section OL-KR4−OL-KR10 at Olkiluoto, Finland," *Explor. Geophys.*, vol. 46, no. 2, pp. 141–152, Jun. 2015, doi: 10.1071/EG13057.
[25] F. T. Ulaby, E. Michielssen, and U. Ravaiol, *Fundamentals of Applied Electromagnetics*, 6th ed. Beijing, China: Tsinghua Univ. Press, 2016.
[26] L. Meng, "Experimental study on the electrical parameters of coal," M.S. thesis, Henan Polytechnic Univ., Jiaozuo, China, 2010.
[27] M. Zhang, "Study on the influence of coal and rock electrical parameters with different frequencies at the radio wave perspective," M.S. thesis, Chongqing Univ., Chongqing, China, 2021.
[28] I. Brach, J. C. Giuntini, and J. V. Zanchetta, "Real part of the permittivity of coals and their rank," *Fuel*, vol. 73, no. 5, pp. 738–741, 1994, doi: 10.1016/0016-2361(94)90017-5.
[29] X. Guo, X. Huan, W. Gong, and Y. Zhang, "Study on coal complex resistivity anisotropy and frequency response characteristics," *Coal Sci. Technol.*, vol. 45, no. 4, pp. 167–170, 2017, doi: 10.13199/j.cnki.cst.2017.04.029.
[30] L. Xu, C. Liu, and X. Xian, "Fractal characteristics of alternating current conductivity of coal," *Coal Convers*, vol. 24, no. 1, pp. 50–52, 2001, doi: 10.3969/j.issn.1004-4248.2001.01.011.
[31] S. Yang, "Experimental study on the electrical parameters of being loaded gas-filled coal," M.S. thesis, Henan Polytechnic Univ., Jiaozuo, China, 2012.
[32] C. Cai et al., "Study on the dielectric properties of coking coal with high sulfur content," *J. China Coal Soc.*, vol. 38, no. 9, pp. 1656–1661, 2013, doi: 10.13225/j.cnki.jccs.2013.09.007.
[33] X. Li, L. Zhang, B. Nie, C. Yang, and F. Zhu, "Law of relative dielectric constant of coal under different stresses and gas pressures," *J. Min. Sci. Technol.*, vol. 3, no. 4, pp. 349–355, 2018, doi: 10.19606/j.cnki.jmst.2018.04.005.
[34] L. Xu, H. Liu, Y. Jin, B. Fan, X. Qiao, and B. Jing, "Structural order and dielectric properties of coal chars," *Fuel*, vol. 137, pp. 164–171, Dec. 2014, doi: 10.1016/j.fuel.2014.08.002.
[35] N. Zhang, L. Cai, J. Xu, R. Wang, and F. Li, "Dielectric properties of Australia lignite at radio frequency," *Energy Sources Part Recovery Util. Environ. Eff.*, vol. 38, no. 6, pp. 828–834, Mar. 2016, doi: 10.1080/15567036.2013.805284.
[36] Q. Wan, "Resistivity and relative permittivity of coal," *Min. Saf. Environ. Prot.*, no. 1, pp. 17–24, 1982.
[37] J. H. Schön, *Physical Properties of Rocks: A Workbook*. Amsterdam, The Netherlands; New York, NY, USA: Elsevier, 2011.
[38] D. K. Cheng, *Field and Wave Electromagnetics*, 5th ed. Beijing, China: Tsinghua Univ. Press, 2013.
[39] X. Ju, *Practical Antenna Engineering Technology*. Xi'an, China: Xidian Univ. Press, 2015.
[40] J. D. Kraus and R. J. Marhefka, *Antennas: For All Applications*, 3rd ed. Beijing, China: Publishing House Electron. Ind., 2017.

Shun Yang received the M.S. degree in safety engineering from Jiangxi University of Science and Technology, Ganzhou, China, in 2021. He is currently working toward the Ph.D. degree in mineral engineering with the School of Resources and Safety Engineering, Chongqing University, Chongqing, China.

His research interests include electromagnetic prospecting theory and applications.

Yanqing Wu received the Ph.D. degree in earth exploration and information technology from Central South University, Changsha, China, in 2002.

He is currently the Professor with the School of Resources and Safety Engineering, Chongqing University, Chongqing, China. He has authored/coauthored more than 55 refereed journal articles. He is an expert in geological disasters for the National Work Group on Safety Production. His research interest includes mining geophysics.

Peng Lu received the M.S. degree, in 2020, in integrated circuit engineering from Chongqing University, Chongqing, China, where he is currently working toward the Ph.D. degree in mineral engineering with the School of Resources and Safety Engineering.

His research interests include virtual-instruments theory, engineering equipment application, and manufacturing.

Zhifang Liu received the M.S. degree in safety engineering from Jiangxi University of Science and Technology, Ganzhou, China, in 2021.

Since 2021, she has been a Lecturer with Institute of Intelligent Manufacturing, Chongqing Vocational College of Light Industry, Chongqing, China. She is currently involved in research on the safety engineering and resource security management.